Investigating energy production and wake losses of multi-gigawatt offshore wind farms with atmospheric large-eddy simulation

Peter Baas[1], Remco Verzijlbergh[1,2], Pim van Dorp[1], and Harm Jonker[1,3]

[1]Whiffle, Molengraaffsingel 8, 2629 JD Delft, The Netherlands
[2]Delft University of Technology, Department of Engineering Systems & Services, Jaffalaan 5, 2628 BX Delft, the Netherlands
[3]Delft University of Technology, Department of Geosciences & Remote Sensing, Stevinweg 1, 2628 CN Delft, the Netherlands

Correspondence: Peter Baas (peter.baas@whiffle.nl)

Abstract. As a consequence of the rapid growth of the globally installed offshore wind energy capacity, the size of individual wind farms is increasing. This poses a challenge to models that predict energy production. For instance, the current generation of wake models has mostly been calibrated on existing wind farms of much smaller size. This work analyses annual energy production and wake losses for future multi-gigawatt wind farms with atmospheric large-eddy simulation. To that end, one
5   year of actual weather has been simulated for a suite of hypothetical four-gigawatt offshore wind farm scenarios. The scenarios differ in terms of applied turbine type, installed capacity density, and layout. The results suggest that production numbers increase significantly when the rated power of the individual turbines is larger, while keeping the total installed capacity the same. Even for turbine types with similar rated power, but slightly different power curves, significant differences in production were found. Although wind speed was identified as the most dominant factor determining the aerodynamic losses, a clear
10   impact of atmospheric stability has been identified. By analyzing losses of the first-row turbines, the yearly average global-blockage effect is estimated between 2 to 3 %, but it can reach levels over 10 % for stably stratified conditions and wind speeds around 8 ms^{-1}. Using a high-fidelity modeling technique, the present work provides insights in the performance of future, multi-gigawatt wind farms for a full year of realistic weather conditions.

1 Introduction

15   As part of the transition to renewable energy sources, the European offshore wind energy capacity is expanding rapidly. For example, the offshore wind energy capacity in Dutch, Belgian, Danish and German parts of the North Sea is anticipated to reach the 65 GW mark in the year 2030 and 150 GW in the year 2050 (The Esbjerg Declaration, 2022) whereas the European-wide target for offshore wind in 2050 is 300 GW (European Commission, 2020).

Ten years ago, the largest offshore wind farms had a capacity of around 500 MW. Nowadays this number has increased to
20   1500 MW and before the year 2030, wind farms of 4000 MW will be no exception. In fact, already today clusters of wind farms with a joint capacity of several gigawatts exist. In parallel, the wind turbines themselves increase in size. The current generation of offshore wind turbines have a nominal power of 10 to 12 MW, but this could increase to as much as 20 MW for

the year 2030. Offshore wind energy is thus entering a new phase on three levels: the total installed capacity, the size of the wind farms and the size of the individual wind turbines.

25   Veers et al. (2019), among others, are pointing out the need for a better understanding of atmospheric flows through wind farms. In particular the growth of wind farm size poses a challenge for models that predict energy production. The current generation of wake models has been extensively validated on wind farms in the 100 MW to 500 MW range. Using these model to make predictions for the future generation of multi-gigawatt wind farms forces them to operate well outside their validation range. This would at least add significant uncertainty to their predictions. It could therefore be argued that more physics-based
30   models have higher fidelity in this 'terra incognita'.

One of such modeling techniques is Large-Eddy Simulation (LES). By numericaly integrating the filtered conservation equations of mass, momentum, temperature, and moisture, LES is able to capture the essential aspects of wind farm flow dynamics in a physically sound way. The 'global-blockage' phenomenon is a fitting exampe: the presence of a wind farm induces spatial gradients in the modeled pressure field, leading to forces upwind of the wind farm, thus 'informing' the flow
35   about the 'obstacle' ahead and causing the flow to deflect (around and/or over the wind farm).

LES has been at the forefront of wind farm flow physics research for some time, see for example the reviews in Mehta et al. (2014), Stevens and Meneveau (2017) and Porté-Agel et al. (2020). Owing to the increase in wind turbine and wind farm scale, a number of recent studies have explored atmospheric flows through large wind farms. Maas and Raasch (2022) have studied the wake effects of a cluster of offshore in the German bight, exploring aspects like (far) wake effects, boundary layer structure,
40   turbulence and entrainment of kinetic energy for a selection of cases with different atmospheric stability. Verzijlbergh (2021) discussed some aspects of modelling flows through large wind farms with illustrative LES results of a 4 GW wind farm in the North Sea.

The present work aims to explore the energy production and internal wake effects for a suite of hypothetical 4 GW offshore wind farm scenarios. The scenarios differ in terms of applied turbine type, capacity density, and layout. Furthermore, we
45   study how wake losses depend on atmospheric stability and we discuss the global-blockage phenomenon. Amongst others, we address questions like: how large are aerodynamic losses in 4 GW wind farms and how do these depend on wind speed, wind direction and atmospheric stability? What is the impact of turbine size and power density? How are losses distributed over the wind farms for different layouts and geometries?

To this end, for a total of six hypothetical wind farm scenarios we simulate one year of actual weather with the GRASP
50   (GPU-Resident Atmospheric Simulation Platform) LES model. This is done by driving the LES with data from ECMWF's ERA5 reanalysis dataset (Hersbach et al., 2020). In this way, we obtain representative distributions of, for example, wind speed, stability, and baroclinicity in a natural way (Schalkwijk et al., 2015b). The resulting dataset can be regarded as a consistent, three-dimensional, one-year dataset of pseudo-observations of meteorological variables (including wake effects) and power production (at turbine level). It allows for a more statistical approach to study wind farm dynamics compared to considering a
55   selection of idealized case studies.

This paper is organized as follows. In Section 2 the model is introduced. The different scenarios are described in Section 3. Section 4 presents the results. After a discussion in Section 5, the Conclusions are summarized in Section 6.

2 Model description and simulation strategy

The model simulations are carried out with the GPU-Resident Atmospheric Simulation Platform (GRASP). GRASP is an LES
60 code that runs almost entirely on GPU's, see Schalkwijk et al. (2012). The origin of GRASP can be traced back to the Dutch
Atmospheric Large Eddy Simulation model (DALES), which is extensively described in Heus et al. (2010).

2.1 Governing equations

We present the most important governing equations below. More details can be found in Heus et al. (2010), Böing (2014)
and Schalkwijk et al. (2015a). We follow Einstein's summation notation, with $x_1, x_2, x_3 = x, y, z$ for the coordinates and
65 $u_1, u_2, u_3 = u, v, w$ for the wind components. The continuity equation reads:

$$\frac{\partial \rho_b u_j}{\partial x_j} = 0 \tag{1}$$

In the anelastic approximation employed in GRASP, the density $\rho_b = \rho_b(z)$ represents a base density profile depending on
height only.

$$\rho_b \frac{\partial u_i}{\partial t} = -\frac{\partial \rho_b u_i u_j}{\partial x_j} - \frac{\partial \tau_{ij}}{\partial x_j} - \frac{\partial p'}{\partial x_i} + \delta_{i3} \rho_b B + \epsilon_{ij3} f_c (u_j - u_{geo,j}) + \left(\frac{\partial \rho_b u_i}{\partial t} \right)_{\text{sources}} \tag{2}$$

70   In the Navier-Stokes equation above, we denote buoyancy with B. The large-scale pressure gradient term has been written
as a geostrophic wind u_{geo}. Further, f_c denotes the Coriolis parameter and p' the pressure fluctuations. The subgrid turbulent
stress, τ_{ij}, needs to be modeled with an appropriate turbulence closure. There is a wide variety of subgrid models, of which a
significant part uses the concept of eddy viscosity:

$$\tau_{ij} = -2 K_m S_{ij}, \tag{3}$$

75 where

$$S_{ij} = \frac{1}{2} \left(\frac{\partial u_i}{\partial x_j} + \frac{\partial u_j}{\partial x_i} \right) \tag{4}$$

is (the symmetric part of) the velocity-gradient tensor.

All rooted in functions of the velocity-gradient tensor, a variety of subgrid-models is available in GRASP, having a form
like:

80 $K_m = (c_s \Delta)^2 f(S_{ij}) \tag{5}$

with a term containing the grid resolution, Δ, a pre-factor, c_s, and some function of the velocity-gradient tensor. The pre-factor
c_s is named after the so-called Smagorinsky-constant in the traditional Smagorinsky subgrid scheme. In this study we apply
the Rozema model (Rozema et al., 2015), which is a minimum-dissipation eddy-viscosity model specifically developed for
anisotropic grids.

Transport of moisture is described by:

$$\rho\frac{\partial q_t}{\partial t} = -\frac{\partial \rho u_j q_t}{\partial x_j} - \frac{\partial F_j^q}{\partial x_j} + S_{q_t}, \tag{6}$$

where $q_t = q_v + q_l + q_i$ denotes the conserved variable total specific humidity, being the sum of vapor, liquid and ice water. Sub-grid fluxes of humidity are denoted F_j^q and other sources of humidity are denoted by S_{q_t}.

Transport of heat is described by:

$$\rho\frac{\partial \vartheta_l}{\partial t} = -\frac{\partial \rho u_j \vartheta_l}{\partial x_j} - \frac{\partial F_j^\vartheta}{\partial x_j} + S_{\vartheta_l}, \tag{7}$$

where the source term is due to radiative transfer. Radiative transfer calculations are carried out off-line based on the ERA5 input profiles of the relevant variables.

We use a temperature,

$$\vartheta_l = \frac{h_l}{c_p} - T_0 \tag{8}$$

that is based on moist static energy h_l:

$$h_l = c_p T + gz - L_v q_l - L_i q_i \tag{9}$$

This is a conserved variable for moist adiabatic ascent. Here $T_0 = 273.16\mathrm{K}$. Further, $c_p = 1005\mathrm{kJkg}^{-1}\mathrm{K}^{-1}$ denotes the specific heat capacity of air (at constant pressure), $L_v = 2.25 \cdot 10^6 \mathrm{Jkg}^{-1}$ the latent heat of vaporization of water, and $L_i = 2.84 \cdot 10^6 \mathrm{Jkg}^{-1}\mathrm{K}^{-1}$ the latent heat of sublimation of ice.

2.2 Boundary conditions

2.2.1 Large-scale NWP

In this study, the LES is coupled to ECMWFs ERA5 reanalysis dataset. As we apply periodic lateral boundary conditions, no large-scale gradients can be resolved by the LES (a model version with open boundary conditions is currently being developed). Instead, large-scale (LS) tendencies are extracted from ERA5 and incorporated in the LES. Therefore, several model terms are adjusted and/or added:

$$\rho_b\frac{\partial u_i}{\partial t} = \cdots + \epsilon_{ij3}f(u_j - u_{geo,j}^{LS}) - \rho u_i^{LS}\frac{\partial u_j^{LS}}{\partial x_j} - w^{LS}\frac{\partial u_i}{\partial z} + \frac{1}{\tau}\left(u_i^{LS} - \overline{u_i}\right) \tag{10}$$

$$\frac{\partial \phi_i}{\partial t} = \cdots - \rho u_i^{LS}\frac{\partial \phi_j^{LS}}{\partial x_j} - w^{LS}\frac{\partial \phi_i}{\partial z} + \frac{1}{\tau}\left(\phi_i^{LS} - \overline{\phi_i}\right) \tag{11}$$

The final terms of Eqs. 10 and 11 represent nudging to the large-scale model: the slab-averaged model fields ($\overline{u_i}$, $\overline{\phi_i}$) are nudged to ERA5 with a nudging time scale, τ, of 6 h. This time scale is short enough to give the LES physics enough freedom to establish its own unique state, but short enought to make the simulation follow slow large-scale disturbances such as weather fronts (Neggers et al., 2012).

2.2.2 Lower boundary conditions

Over water surfaces (as in the present study), GRASP uses a prescribed surface temperature T_s. At the surface, saturation is assumed:

$$q_{ts} = q_{sat}\left(T_s, p_s\right) \tag{12}$$

The surface roughness lengths for momentum and heat, $z_{0m,h}$ are parameterized following the ECMWF IFS documentation ECMWF (2017):

$$z_{0m} = \alpha_m \frac{\nu}{u_*} + \alpha \frac{u_*^2}{g} \tag{13}$$

$$z_{0h} = \alpha_h \frac{\nu}{u_*} \tag{14}$$

where is α the Charnock parameter, taken as 0.0185. Furthermore, $g = 9.81\mathrm{ms}^2$ is the gravitational constant; $\nu = 1.5 \cdot 10^{-5}\mathrm{m}^2\mathrm{s}^{-1}$ is the kinematic viscosity of air, $\alpha_m = 0.11$ and $\alpha_h = 0.4$. For momentum, this parameterization follows Charnock (1955) added with viscous effects for light wind conditions.

2.2.3 Lateral boundary conditions

In the present set-up we apply periodic boundary conditions. To prevent the recirculation of wind farm wakes, we make use of a concurrent-precursor simulation Stevens et al. (2014). This is a simulation without wind turbines that runs in parallel with the 'actual' simulation. Over the boundary region the values of the 'actual' simulation are nudged towards the precursor simulation. A schematic overview of this set-up is shown in Fig. 1.
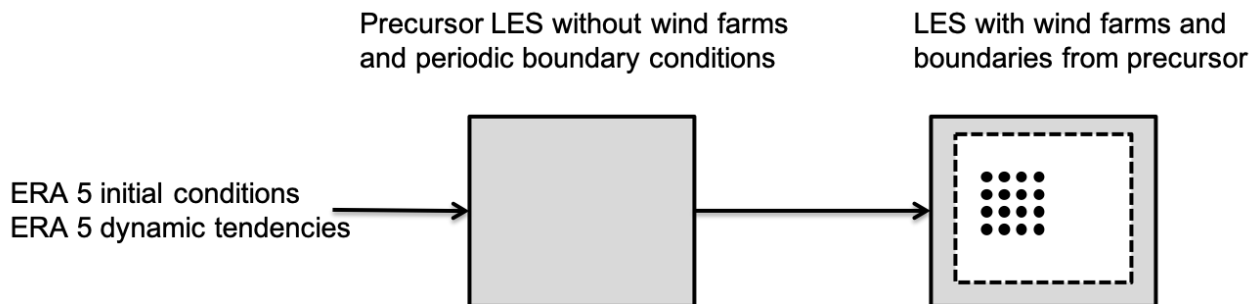
Figure 1. Schematic view of ERA5 boundary conditions, a precursor simulation, and a nested domain with turbines.

2.3 Wind turbine parameterization

Wind turbines are modeled by a so-called actuator disk model. This models each turbine as a semi-permeable disk that exerts
130 forces on the flow that are consistent with the thrust curve of the wind turbine. In this way, wind farm wake effects are taken
into account. In addition, using the turbine power curve, the turbine parameterization allows to directly model power output
per turbine on a high temporal resolution. The actuator-disk model is implemented following Meyers and Meneveau (2010)
and Calaf et al. (2010). Within this parameterization, the total drag force exerted on the flow by a wind turbine is modelled as

$$F_t = -\frac{1}{2}\rho A C_t' \overline{M_D}^2 \tag{15}$$

135   where ρ is the air density, $A = \pi R^2$ is the frontal area of the rotor and C_t' the thrust coefficient based on the disk-averaged
wind speed $\overline{M_D}^2$. Wind turbine power is given by

$$P_t = -\frac{1}{2}\rho A C_p' \overline{M_D}^3 \tag{16}$$

with C_p' the disk-based power coefficient. The disk-based power and thrust coeffients are determined from the manufacturers
power- and thrustcurves by means of an offline simulation. This additional step is required since the manufactorer curves are
140 based on a free-stream wind speed, $\overline{M_\infty}$, a reference density, ρ_0, and a reference turbulent intensity, TI_{ref}. An additional ad-
vantage of this approach is that the turbines by definition produce the correct power and thrust for the given grid configuration.
The present implementation of the actuator-disk model has been tested extensively in operational practice and shows good
performance for a wide range of numerical grid settings.

In order to quantify wake losses, we compare the energy production of the wind turbines with the production of so-called
145 thrustless turbines. These thrustless turbines are embedded in the concurrent-precursor simulation. The disk-based power co-
efficients for the thrustless turbines are obtained by setting the thrust coefficient to 0. As a result, a power production of the
thrustless turbines can be determined, but they do not excert drag on the flow. Thus, each thustless turbine produces power
as if it were a single isolated turbine. Furthermore, the simulations with thrustless turbines and those with the active turbines
experience exactly the same turbulent wind fields at the boundaries. As such, the difference between the production of the
150 thrustless turbines and the active turbines is a measure of the aerodynamic loss.

2.4 Simulation strategy

For each of the wind farm scenarios (Sect. 3.1), the year 2015 was simulated. The year-long simulations consist of concatenated
daily simulations with a spin-up of 2 hours. For each day, GRASP is initialized at 22 h (UTC) the previous day. Model output
valid between 0 and 24 h (UTC) is used for the analysis.
155   The model domain consists of 640 x 640 x 48 grid points. The horizontal grid spacing is 120 m, the lowest grid box has a
height of 30 m. The horizontal domain size extends to 76800 m. Vertical grid stretching was applied to obtain a domain height

of 3000 m. The model domain is centered around 52.8659° N and 3.5364° E. This corresponds to a location in the North Sea, roughly 100 km from the Dutch coast witin the planned 4000 MW wind farm IJmuiden Ver. Also, the metmast 'Meteomast IJmuiden', which was operational during 2015, is located in the domain.

160   Compared to other LES studies (cf. Wu and Porté-Agel (2017), Maas and Raasch (2022), Strickland et al. (2022)), the horizontal resolution of 120 m is relatively coarse. This choise results from a trade-off between computational cost and accuracy and has been tested extensively in an operational setting. As such, it follows from our ambition to simulate a full year of realistic weather conditions, rather than the common approach of running a suite of targeted (idealized) case studies. To provide insights into the effect of the applied resolution, the sensitivity of the results to the grid spacing are discussed in the discussion section.

165   As a basic validation of the model's capability to represent the local wind conditions, Figure 2a compares modeled versus observed wind speed at a height of 92 m. The correspondence between model and tower observations are satisfactory, with error metrics within the expected range for wind resource assessments. Figure 2b shows the distribution of the modeled 92 m wind speed, with a Weibull function fitted to the data. For comparison, grey dots indicate the distribution of the observations. Figure 2c presents the (modeled) wind rose, indicating that south-westerly winds have the highest frequency of occurrence and

170   are generally stronger than winds from other sectors.
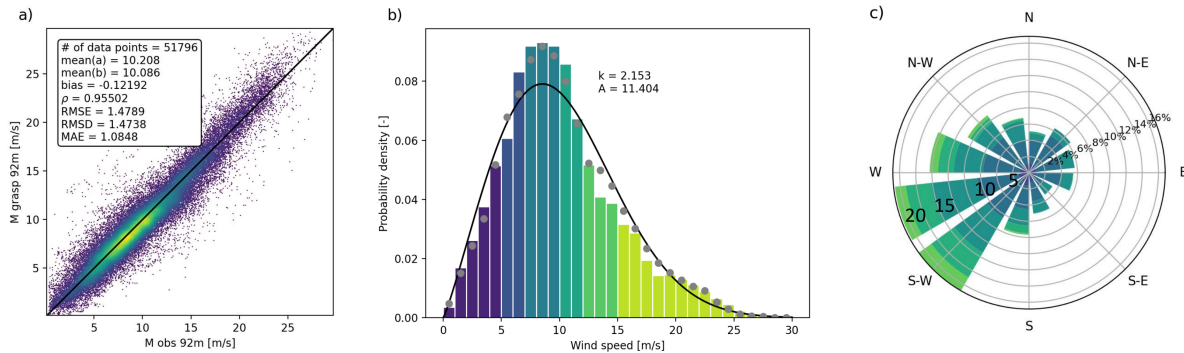
Figure 2. Validation results of GRASP vs. offshore tall mast IJmuiden. a) Modeled versus observed wind speed at 92 m. b) Weibull plot of GRASP 92m wind speed. Grey dots represent the observations. c) Modeled wind rose at 92 m. Colors indicate 5 ms^{-1} intervals.

3 Wind farms scenarios and turbine characteristics

In this Section, the six hypothetical 4000 MW wind farm scenarios and details of the applied turbine types wil be introduced.

3.1 Scenarios

Layouts of the six considered scenarios are given in Fig. 3. The rationale for the first five scenarios is the same: each layout consists of four sites of roughly 10 by 10 km, separated by 3 km wide corridors. Each of the four sites within each scenario

has an installed capacity of approximately 1000 MW (Scenario 1 to 4). The number of turbines depends on the rated power of the applied turbine. As Scenario 5 has only half the capacity density of the other Scenarios (5 MW.km^{-2} instead of 10 MWkm^{-2}), each of its four sites have only half the installed capacity (i.e. 500 MW). Scenario 6 is based on the actual site boundaries of the planned IJmuiden Ver wind farm for which a tender is expected to open in 2023 RVO (2022). The installed
180   capacity of 4000 MW corresponds to the actual plans.
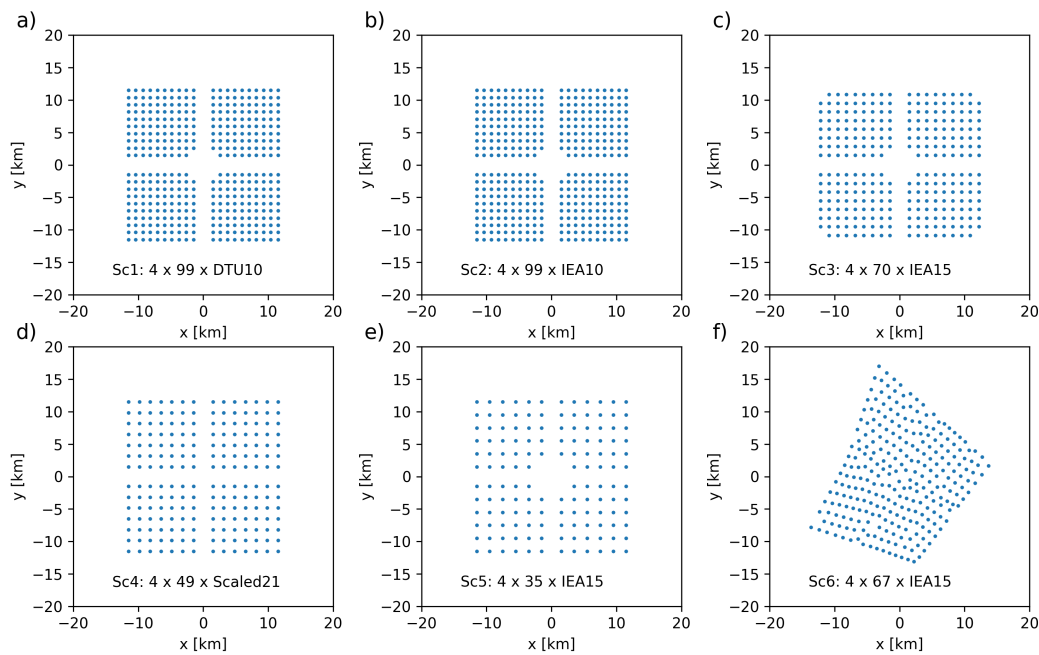
Figure 3. Layouts of the six 4 GW wind farm scenarios.

3.2   Turbine types

To study the impact of using different turbine types while keeping the total installed power approximately the same, four different turbine types are used. Their rated power ranges from 10.6 MW to 21.4 MW. Power- and thrustcurves are given in Fig. 4. Except for the 21.4 MW turbine, all data are taken from reference wind turbines, as published on https://nrel.github.io/turbine-
185   models/Offshore.html. The 21.4 MW turbine, labeled Scaled21, was constructed by using the same power and thrust curves as the IEA15 turbine but increasing the rotor diameter to obtain the desired rated power. The rated wind speed of the IEA10 is lower then the DTU10. Instead, the latter produces lower thrust. Differences between the c_p and c_t curves of the IEA10 and IEA15 turbines are small.
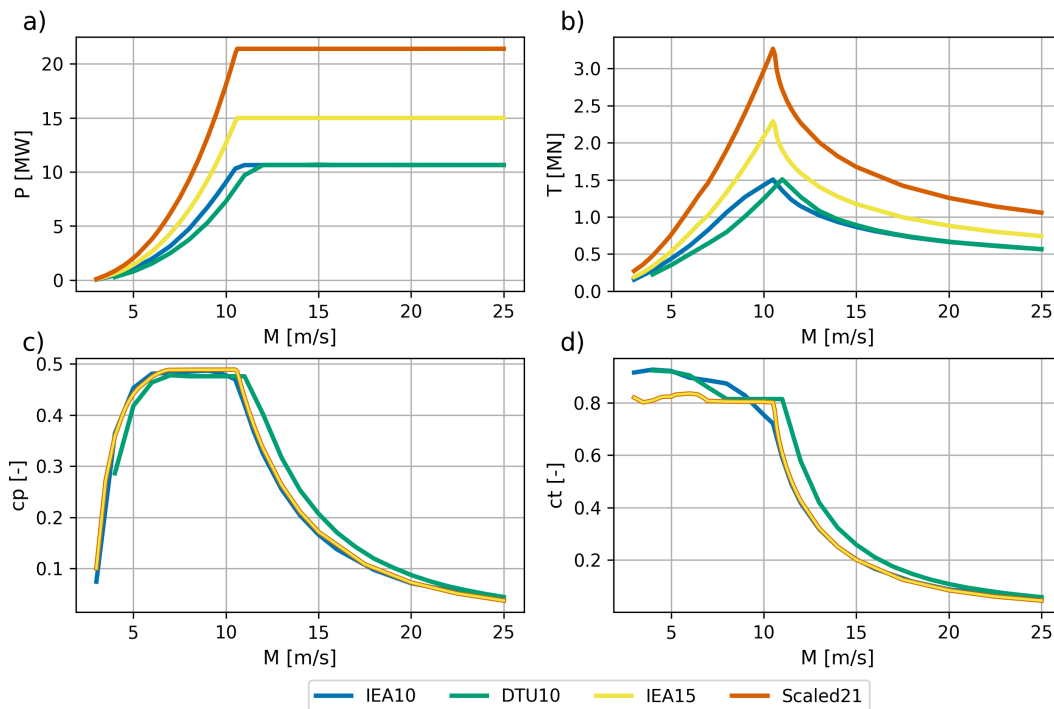
Figure 4. Power and thrust curves for the applied turbine types.

An overview of the scenarios and turbine characteristics is given in Table 1. The installed capacity of the first four scenarios
is close to 4200 MW. For Scenario 5, with half the capacity density, this is 2100 MW. The installed capacity for the IJmuiden
Ver scenario (Scenario 6) is a little lower than the other scenario's. Turbine spacing is between 5.6D and 6.2D for the 10
MWkm^{-2} scenarios and 8.3D for the 5 MWkm^{-2} scenario. These values are in the range of values that occur in existing
offshore wind farms. The baseline capacity density of 10 MW/km2 corresponds to the target set for future wind farms in the
Dutch part of the North Sea. In the following, we consider Scenario 3 as a reference, for which more detailed analyses will be
presented.

4 Results

In this Section we discuss the differences in energy production between the six scenarios. We distinguish between production of
the thrustless turbines (also called 'free-stream production' or 'gross power') and actual production ('net power'). We designate
the difference between the two as 'aerodynamic losses'. After analyzing the dependence of the aerodynamic losses on the wind
speed, we discuss the impact of atmospheric stability. Next, losses of the first-row turbines (i.e. turbines which have no other
turbines upsteam) will be considered, which gives an indication of the impact of blockage effects. We will also break down our

Scenario	Turb. type	Short	Hub height [m]	r [m]	P_{rated} [WM]	N [−]	$P_{installed}$ [MW]	Spacing	Density [MWkm^{-2}]
1	DTU_10MW_178RWT	DTU10	119	89	10.6	396	4198	6.2D	10.5
2	IEA_10MW_198RWT	IEA10	119	98	10.6	396	4198	5.6D	10.5
3	IEA_15MW_240RWT	IEA15	150	120	15.0	280	4200	5.6D	10.5
4	Scaled_21.4MW_WT	Scaled21	173	143	21.4	196	4194	5.8D	10.5
5	IEA_15MW_240RWT	IEA15	150	120	15.0	140	2100	8.3D	5.4
6	IEA_15MW_240RWT	IEA15	150	120	15.0	268	4020	5.3D	10.4

Table 1. Overview of the six scenarios, including turbines characteristics. Turbine radius is denoted by r, P_{rated} denotes the turbine rated power, $P_{installed}$ the wind farm installed capacity, and N the number of installed turbines. Turbine spacing is given in number of rotor diameters, D.

results for bins of wind direction. Apart from showing the impact of wind farm layout, this illustrates that for understanding directional differences a proper separation of the wind speed effect and the stability effect is crucial. Finally, we illustrate the results with a selection of composite maps showing variations of wind speed and aerodyanmic losses over the wind farms.

205 Figure 5 presents the overall energy production and the aerodynamic losses for each of the six scenarios. The aerodynamic losses vary between 12 % and 18 % for the 4 GW wind farms whereas the 2 GW variant has losses around 6 %. Several noticable differences between the scenarios become apparent.
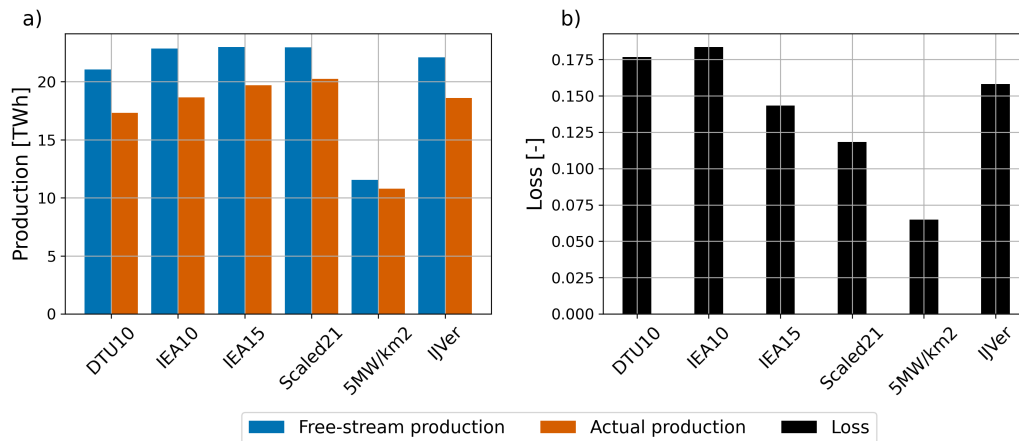
Figure 5. Total free stream and actual production (a) and aerodynamic losses (b) for the six scenarios.

First, although the DTU10 and IEA10 turbine have the same rated power, the actual production of the IEA10 turbine is 7.7 % larger. This significant difference is the result of higher 'free-stream' production numbers. These more than compensate for 210 the slightly higher aerodynamic losses. Both the higher production and the higher aerodynamic losses for the IEA10 scenario can be related to behavior of the respective power curves (see Figure 4).

Second, while keeping the same installed power, it appear to pay-off to apply less but more powerful turbines. This is shown by comparing the IEA10, IEA15, and Scaled21 scenarios. While these three scenarios have similar 'free-stream' production, their actual production varies significantly: for IEA10, production is 5.3 % less than for IEA15, for Scaled21 the production is 2.8 % more. In terms of aerodynamic losses, this implies a reduction from 18.4 % for IEA10 to 11.8 % for Scaled21. At the same time, Table 1 indicates that the turbine spacing in terms of rotor diameters is approximately the same for these three scenarios. This suggests that the (relative) reduction of the number of turbines that is hampered by wakes of other turbines is a major factor contributing to higher production (for instance, the ratio of the number of first-row turbines over 'wake-impacted' turbines will increase (beneficial) when the total number of turbines becomes smaller).

Third, Fig. 5 illustrates the impact of varying the installed capacity per square kilometer. As expected, in the 5 $\mathrm{MWkm^{-2}}$ scenario, the free-stream production is reduced by 50 % compared to the reference IEA15 scenario. However, the actual production decreases only by 45.2 %. The aerodynamic losses decrease drastically from 14.3 % to 6.5 %.

Fourth, the results of the IJVer scenario are comparable to the IEA15 scenario. Its free-stream production is a bit less, because the installed capacity is slighty lower. Also, its aerodynamic losses are slightly higher, which is mainly related to the absence of the 3 km wide corridors (see Fig. 3).

In summary, the present results indicate that expected aerodynamic losses for a 4 GW offshore wind farm are in the range of 12 to 18 %, where the exact value is determined by the rated power of the applied turbines (or: the number of installed turbines). Moreover, turbines of the same rated capacity but different power curves may give significantly different production numbers. We emphasize that absolute numbers are related to the prevalent wind conditions in the simulated year 2015. To obtain AEP estimates that are representative for a longer period, addditional statistical postprocessing of the data are required, but this is out of the scope of the present work.

4.1 Wind speed-dependence of production and losses

Figure 6 considers energy production and aerodynamic loss as a function of the free-stream disk-averaged wind speed (i.e. the disk-averaged wind speed from the thrustless turbines in the concurrent precursor simulation). From left to right, the top panels represent instantaneous wind farm production, total production, and cumulative production, respectively. The bottom panels show the equivalent aerodynamic losses. The results presented here are representative for the wind climate and the specific turbine design choices. A few interesting observations can be made.

First, Fig. 6a indicates that for wind speeds stronger than 14 $\mathrm{ms^{-1}}$ all scenarios operate at rated power. For these strong wind conditions, which generate 50 % of the total energy production (Fig. 6c), the energy content of the flow is so large that aerodynamic losses are negigible.

Second, Fig. 6d,e,f illustrate that 80 % of all aerodynamic losses occur within a narrow wind-speed range of 8 to 12 $\mathrm{ms^-1}$. For lower wind speeds production and losses are low anyway, for higher wind speeds all turbines operate at (or close to) rated power. Around cut-out winds speed substantial instantaneous negative losses occur (Fig. 6d). This remarkable feature is caused by the fact that for these wind speeds, as a result of subtle wake effects, the number of power-producing turbines in the simulations with actual (thrust-generating) turbines is larger than in the simulations with the thrustless turbines. As the
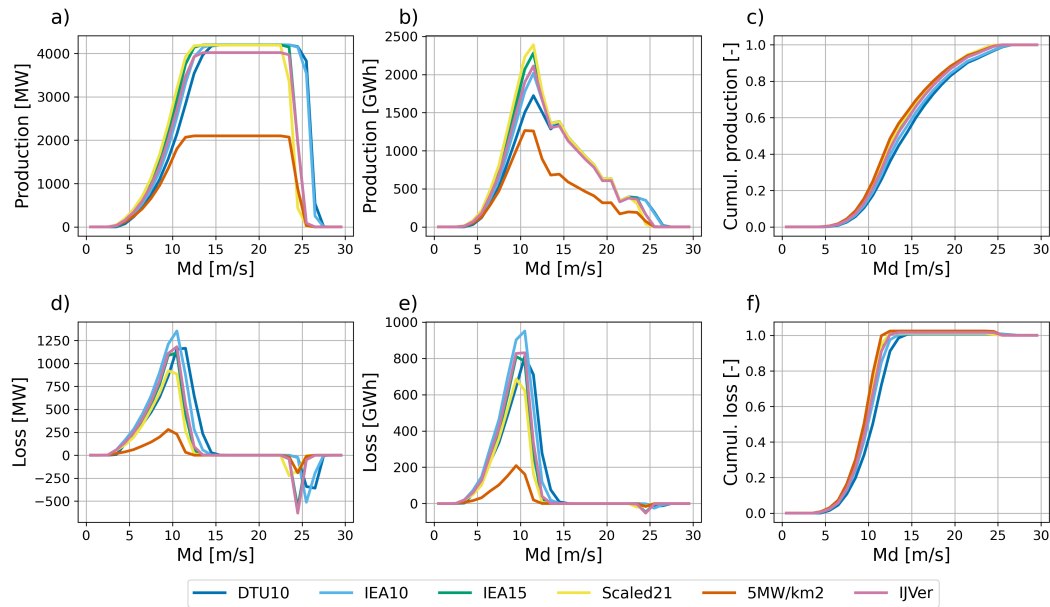
Figure 6. Top: wind farm power production (a), total energy production (b), and cumulative production (c) as function of the free-stream disk-averaged wind speed. Bottom: wind farm power losses (d), total aerodynamic losses (e), and cumulative losses (f) as function of the free-stream disk-averaged wind speed.

frequency of occurrence of these specific wind conditions is low, the impact this effect on the integrated losses is small (Fig. 6e).

Third, the total energy production peaks around a wind speeds of $12 \, \mathrm{ms^{-1}}$. This can be understood by interpreting the total energy production as a function of wind speed as the convolution of the wind speed probability density (Fig. 2b) and the power curves.

Differences between the six scenarios are small. They are consistent with the total production numbers of Fig. 5 and can be explained by the differences in the turbine power curves (Fig. 4).

4.2 Impact of stability

The impact of atmospheric stability on wake losses of wind farms has been widely reported in the scientific literature, see e.g. Stevens and Meneveau (2017). In this sub-section, we attempt to isolate the impact of stability from the impact of the wind speed itself. For clarity reasons, mainly results for the IEA15 reference scenario are presented.

As a stability parameter, we choose the bulk Richardson number, R_b, over the rotor blade of the IEA15 turbine, i.e. between heights of 270 and 30 m:

$$R_b = \frac{g}{\vartheta_l} \frac{\Delta z \Delta \vartheta_l}{(\Delta u)^2 + (\Delta v)^2}.$$
(17)

260   We consider three classes of stability, separated by the 33.3[th] and 66.6[th] percentiles of the year-round distribution of R_b, which have values of -0.04 and 0.44, respectively. As such, the stability class with the 33.3 % of lowest R_b values represents unstable conditions, while the class with the 33.3 % of highest R_b values represents significantly stable conditions. The class of intermediate stability contains neutral conditions, but is dominated by weakly-stratified conditions.
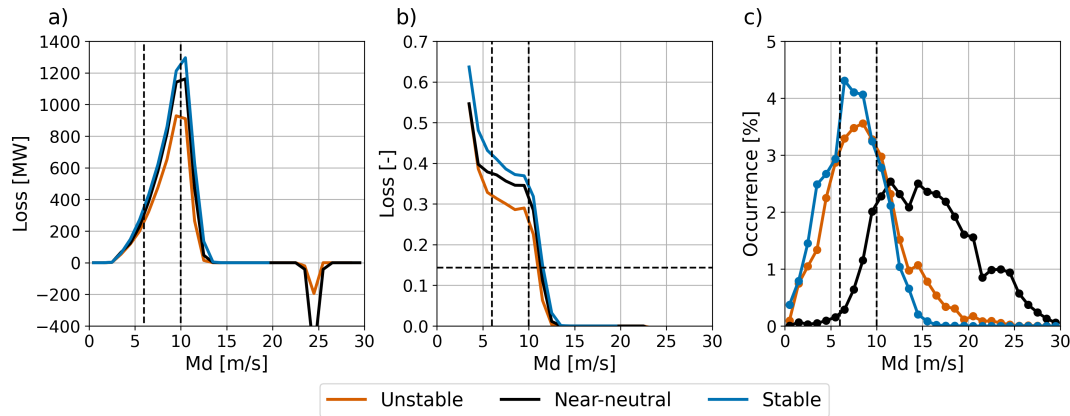
Figure 7. Combined effect of wind speed and stability on wind farm aerodynamic losses. a) Power losses in MW. b) Fractional aerodynamic losses. c) Fequency of occurrence of the three stability classes.

Figure 7 presents the aerodynamic losses as a function of the free-stream disk-averaged wind speed for the three stability
265   classes for the IEA15 scenario. For a wide range of wind conditions, the impact of stability is small. However, just in the wind speed range where most of the actual losses occur, a clear impact of stability is observed. Here, for the most stably-stratified conditions, relative losses are roughly 10% larger than for convective conditions. For higher wind speeds, losses quickly reduce to zero, irrespective of stability. For lower wind speeds, absolute losses (and production) are small.

The strong dependency of aerodynamic losses on the wind speed may easily obscure an analysis to the impact of stabity. The
270   relevant wind speed range for considering the impact of stability seems to be between 6 and 10 ms^{-1}. This narrow range of wind speeds is characterized by near-constant relative losses, which allows for a fair comparison between stability conditions. As can be seen in Fig. 4, this specific wind speed range coincides with the power and thrust curves being at their maximum. In the following, to indicate any impact of stability, we include only data for which the wind speed is between 6 and 10 ms^{-1}.

Table 2 summarizes the fractional aerodynamic losses for all six scenarios for disk-averaged wind speeds between 6 and 10
275   m/s. Considerable differences between scenarios exists: the higher the overall aerodynamic losses (cf. Fig. 5), the larger the impact of stability. For example, the impact of stability is clearly smaller for Scaled21 and 5 MWkm^{-2} scenarios.

Scenario	Unstable	Neutral	Stable
DTU10	0.29	0.37	0.45
IEA10	0.34	0.41	0.48
IEA15	0.29	0.35	0.38
Scaled21	0.26	0.29	0.32
MW/km2	0.14	0.18	0.20
IJVer	0.32	0.36	0.41

Table 2. Fractional aerodynamic losses per scenario for free-stream disk-averaged wind speeds between 6 and 10 m/s, for the three stability classes.

To summarize, the impact of stability is only significant for a small range of wind speed conditions. However, it is exactly this range that is also most relevant for aerodynamic losses.

4.3 First-row losses

280 As with any obstacle placed in a flow, wind farms will have an impact on the flow itself. The air will tend to flow around and over the 'obstacle', and in front of the wind farm a reduction in wind speed is expected. This will lead to a reduction of power production of the turbines that are not in the wake of other turbines (i.e. located at the 'first-row'). This phenomenon is know as the global-blockage effect Bleeg et al. (2018). As the wind speed reduction will propagate to downstream ('waked') turbines, separating the blockage effect from wake effects is virtually impossible. This is especially true for observations and 285 physically-based modeling studies like LES. Therefore, in this study we focus on losses of the first-row turbines, which can be interpreted as a conservative estimate for the blockage effect.

We determine the first-row losses as follows: given the wind direction, for each time step we verify if any other turbines are located within a 60 degree wide sector opposite to the flow direction. If this is not the case, a turbine is classified as a first-row turbine for that particular timestep.

290 Figure 8 presents the year-round production numbers and aerodynamic losses for the first-row turbines and all other ('waked') turbines. The actual production of the first-row turbines is between 2 and 3% lower than their corresponding thrustless (or free-stream) production. Although the applied definitions and metrics can be discussed, these values are not inconsistent with values of the blockage effect reported in literature (e.g. Wu and Porté-Agel (2017), Bleeg et al. (2018), Schneemann et al. (2021), . Consistently, the losses of the non-first-row, or other turbines, is a bit higher than the overall losses.

295 As with the overall aerodynamic losses above, we can also assess the impact of both wind speed and stability on the first-row losses. Figure 9 shows that, consistent with the above results (eg Fig. 6), also the first-row losses are negligible for wind speeds over 12 m/s. Interestingly, the reduction of the first-row wind speed continues for much higher wind speeds. The majority of the first-row losses occur for wind speeds between 6 and 10 m/s. Values range from 4 % in convective conditions to 8 % in the most stable conditions. The corresponding first-row wind speed deficits vary from approximately 0.12 to 0.30 $\mathrm{ms^{-1}}$. Relative 300 first-row losses are even higher for wind speeds below 6 $\mathrm{ms^{-1}}$, but these are less relevant in an absolute sense (not shown).
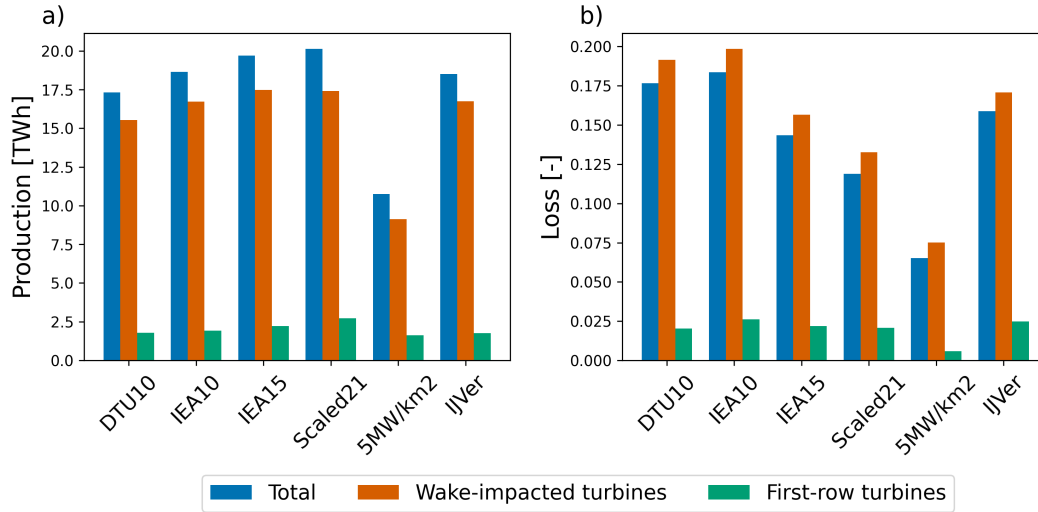
Figure 8. a) Total production, production of 'wake-affected' turbines, and production of first-row turbines for all six scenarios. b) Aerodynamic losses.

We conclude that first-row losses are on average between 2 and 3 %. However, for the wind speed range where most of the losses occur these numbers can be more than twice as high. Also, first-row losses are significantly larger for stably-stratified condions (cf Strickland et al. (2022)).
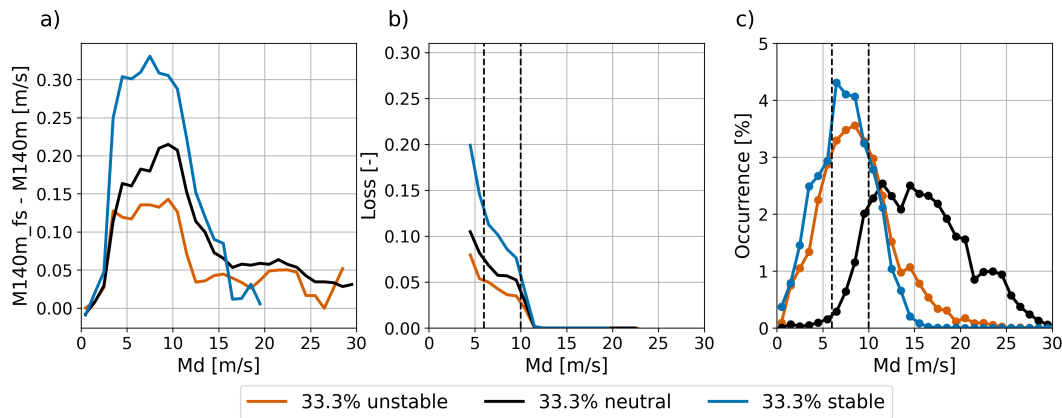
Figure 9. Dependence of first-row wind speed deficits and first-row production losses as a function of wind speed and stability. a) Reduction in wind speed of first-row turbines compared to free stream wind speed. b) First-row losses. c) Frequency of occurrence.

4.4 Directional effects

305 An analysis of aerodynamic losses per wind direction reveals how the respective impacts of wind speed and stability are entangled. Moreover, it shows the impact of difference in layout and geometry of the wind farm scenarios.
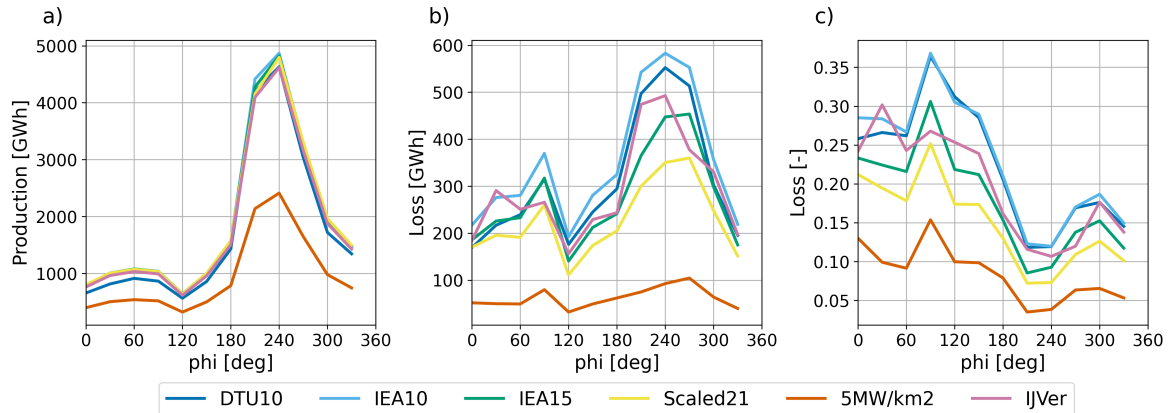
Figure 10. Directional dependence of total energy production (a), absolute aerodynamic losses (b) and relative losses (c) for the six scenarios.

Figure 10 shows energy production and aerodynamic losses as function of the wind direction. The first element that stands out is the overwhelming dominance of the contribution of southwesterly winds to the total energy production. This is the cumulative effect of both the higher frequency of occurrence and the generaly stronger wind speeds (cf. Fig. 2c), in combination

310 with strongly non-linear character of the turbine power curves.

Figure 10b,c show that while the absolute losses are largest for southwesterly direction, the relative losses are much higher for easterly directions. From this Figure, it cannot be determined if the difference in relative losses is mainly a wind speed effect or that stability is important here. Interestingly, the five hypothetical layouts closely follow the same pattern, but the IJVer scenario behaves differently. Comparison with Fig. 3 suggests that this difference is related to the different layout of the

315 IJVer scenario: while other scenarios form north-south, west-east facing squares, the IJVer layout is significantly rotated (but still resembling a clear 'square-like' shape). Inspection of Fig. 10b,c indicates that aerodynamic losses are higher/lower when the flow is directed towards the faces/corners of the wind farm layouts.

For two of the scenarios, IEA15 and IJVer, Fig. 11 breaks down the directional losses to stability and wind speed. The top panels (a, b) present the fractional aerodynamic losses for the three stability classes defined above, irrespective of the wind

320 speed. Losses for stably-stratified conditions are largest, but also the losses for convective conditions are large. Because of generally higher wind speeds (i.e. lower thrust coefficients), the losses for the near-neutral class are much smaller, even when omni-direction numbers are considered (not shown).

As a next step, the bottom panels of Fig. 11 present stability dependant losses like before, but now only inlcluding wind speeds between 6 and 10 ms^{-1}. By doing so, a clear organization of the data occurs, with the lowest losses occurring for

325 convective conditions and the highest losses for the most stably-stratified condition. Moreover, a clear directional pattern is
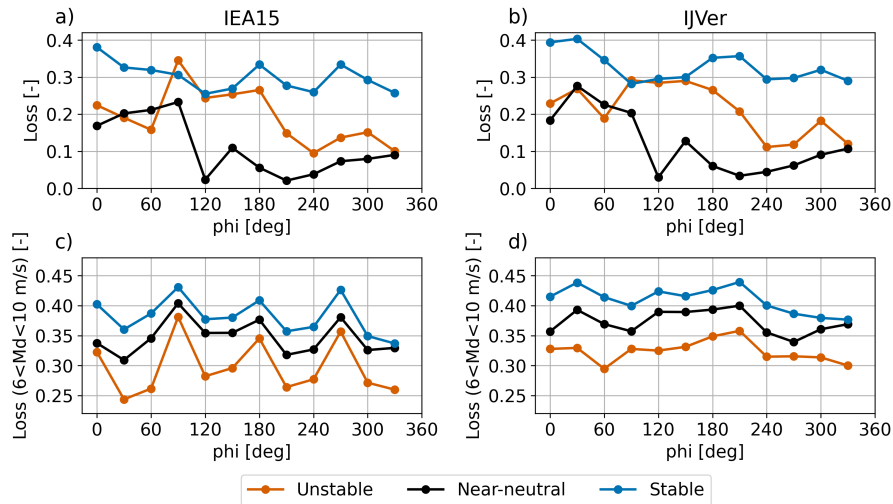
Figure 11. Directional dependence of total aerodynamic losses for different stability classes for the IEA15 (a,c) and IJVer (b,d). The top panels (a,b) are based on all data, the bottom panels (c, d) only include wind speeds between $6\,\mathrm{ms^{-1}}$ and $10\,\mathrm{ms^{-1}}$.

revealed, in particular for the IEA15 scenario, with much higher losses when the flow is directed to the sides of the wind farm and lower losses when the flow faces the corners of the wind farm. This pattern is clearly visible for all three stability classes. For the IJVer scenario the directional pattern is more obscured.

In summary, Fig. 11 demonstrates that an assessment of the impact of stability (a, b) on wind farm losses is not straight-
330 forward. It can only be isolated if the data are also conditioned over a particular, carefully selected wind speed range. This is because both the turbine thrust curves and the stability are depending on the wind speed, but in a different way. To avoid the impact of wind speed as much as possible, this range should not be too broad, as small differences in wind speed can have a large impact on both absolute and relative aerodynamic losses (Fig. 7).

4.5 Spatial patterns

335 So far, we only considered power production and aerodynamic losses for the wind farms as a whole. In the following section, we consider spatial variations in wind speed, power production, and aerodynamic losses over the wind farms. By breaking down the dataset into bins of wind direction, wind speed, and stability classes, the impact of different atmospheric conditions can be examined. A selection of composite maps of aerodynamic losses, wind speed, and the ratio of actual to free stream wind speed (taken from the precursor simulation) are presented.

340 Figure 12 shows aerodynamic losses, mean wind speed and velocity deficit compared to the free-stream flow for the IEA15 scenario, averaged over all the entire year and all wind directions. Losses vary from around 6 % for turbines located at the outside of the wind farm, to 20 % for turbines in the interior of the wind farm. The dominance of stronger southwesterly winds is reflected in lower losses in the southwestern part of the wind farm and a clear asymmetry in the composite wind fields. The
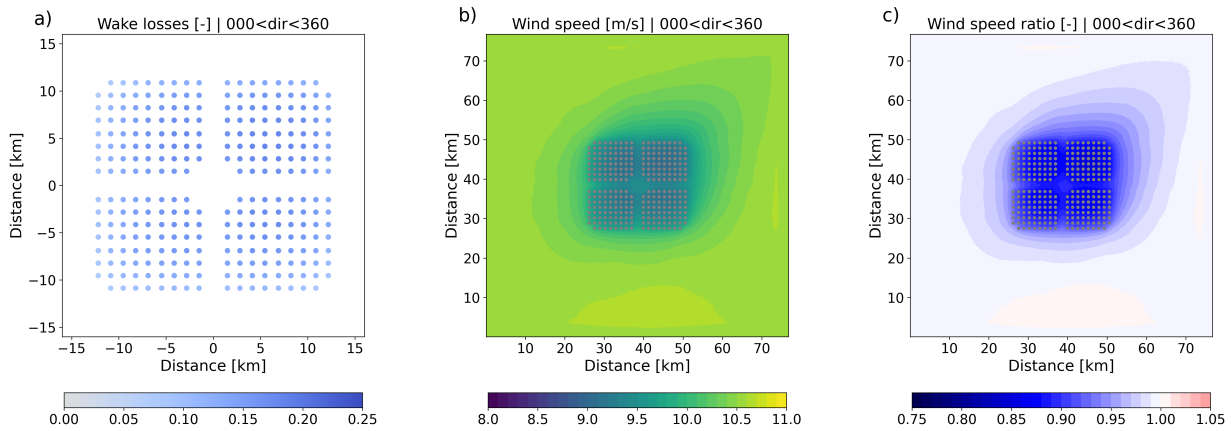
Figure 12. Aerodynamic losses (a), mean 140 m wind speed (b), and ratio of actual to free stream wind speed (c) for the IEA15 scenario (including all data).

impact of the wind farm on the year-round, omni-directional wind field is in the order of 20 km, after which a velocity deficit

345 of less than 1 % is observed.
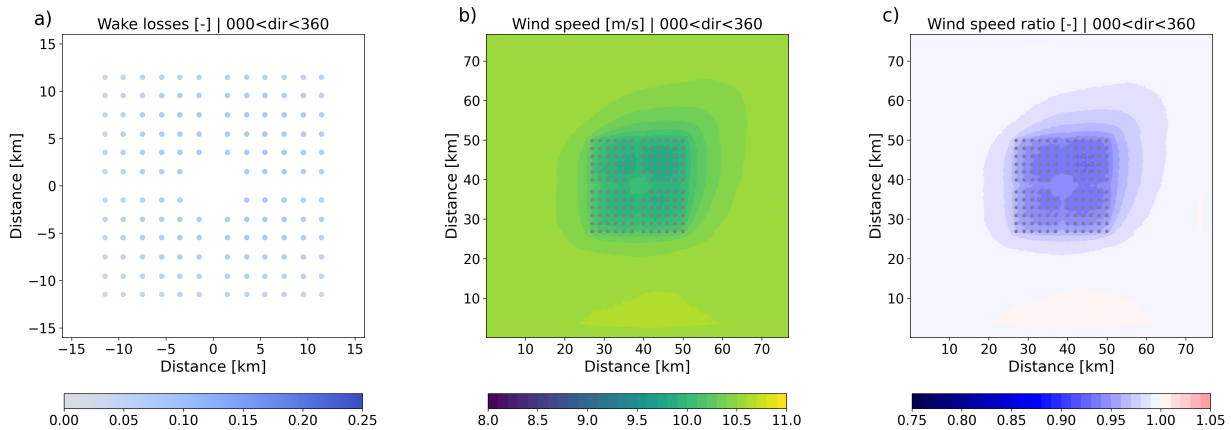
Figure 13. As Fig. 12, but for the 5 $\mathrm{MWkm^{-2}}$ scenario (including all data).

For comparison, Fig. 13 shows the results for the 5 $\mathrm{MWkm^{-2}}$ scenario. As expected, losses are much lower than compared to IEA15, which has a capacity density of around 10 $\mathrm{MWkm^{-2}}$. This is the combined effect of larger distance between the turbines and the fact that only half the number of turbines is involved. The impact on the mean wind field and the corresponding

velocity deficit is smaller as well: in the centre of the wind farm the velocity deficit is 6 %, compared to 12 % in the 10
350   $\mathrm{MWkm^{-2}}$ case.

Figure 14 presents composite maps for the IEA15 scenario again, but now only including data with a wind direction between
15 and 45 degrees. In this case, a clear wake is visible, which is still present as the flow reaches the southern edge of the
domain. Clearly, for studying wake lengths behind wind farms of this size, much larger domains are required than the present
80 kilometers. Upstream, the wind speed is already reduced before the flow reaches the wind farm, which signals the presence
355   of blockage. Along the sides, a clear flow acceleration is visible. The distribution of aerodynamic losses over the wind farm
shows interesting patterns. Although not in the wake of any other turbines, the first-row turbines in the northeastern corner
of the wind farm produce 10 % less power than their 'thustless' equivalents. On the other hand, the turbines in the southeast
profit from the flow acceleration around the wind farm and produce up to 5 % more power than if they would have operated in
isolation.
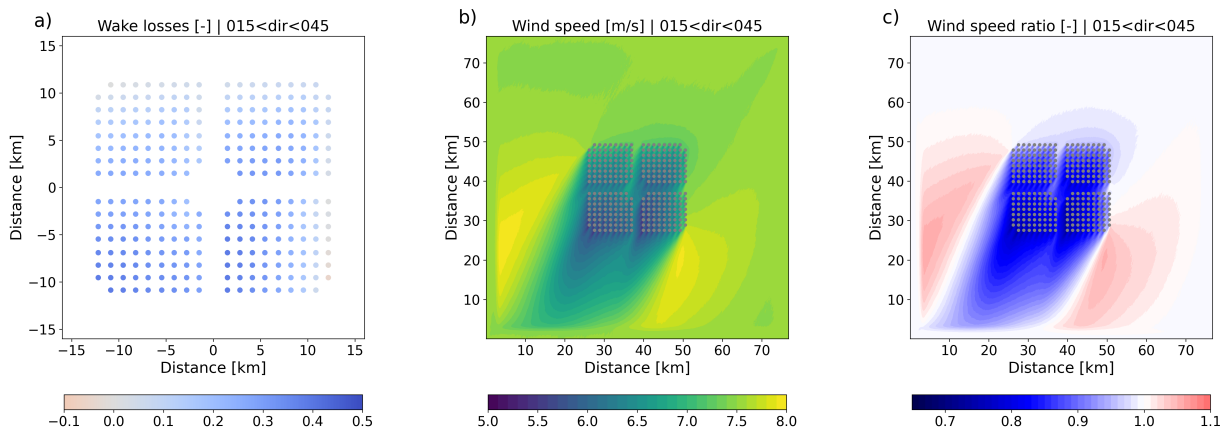
Figure 14. As Fig. 12, but only including wind directions between 15 and 45 degrees.

360   Comparison of Fig. 14 with Fig. 15 clearly illustrates the difference of the flow being oriented to the corner of the wind farm
or directly towards the one of the sides. In case of the latter, the numbers of turbines that are facing undisturbed conditions
(apart from blockage effects) is much less, resulting in larger aerodynamic losses (cf. Fig. 11).

The different layout of the IJVer scenario, makes that aerodynamic losses are relatively low for easterly flow (Fig. 16).
Also here, flow acceleration around the wind farm leads to increased production for, in this particular case, the northernmost
365   turbines.

Finally, Fig. 17 and Fig. 18 illustrate the impact of unstable and stable conditions, respectively. To enable a 'fair' com-
parison, only conditions with wind speeds between 6 and 10 $\mathrm{ms^{-1}}$ are included. As shown before, in this wind speed range
the aerodynamic losses are much higher than average. In stably-stratified conditions deeper wakes occur that extend further
downstream. Also, the wind speed reduction upstream of the wind farm is larger in stable conditions. This is reflected in larger
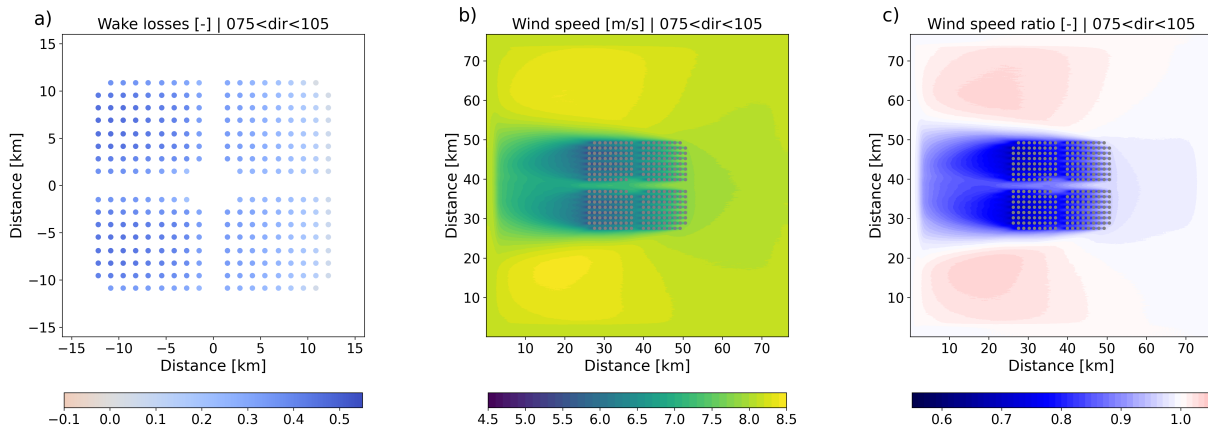
Figure 15. As Fig. 12, but only including wind directions between 75 and 105 degrees.
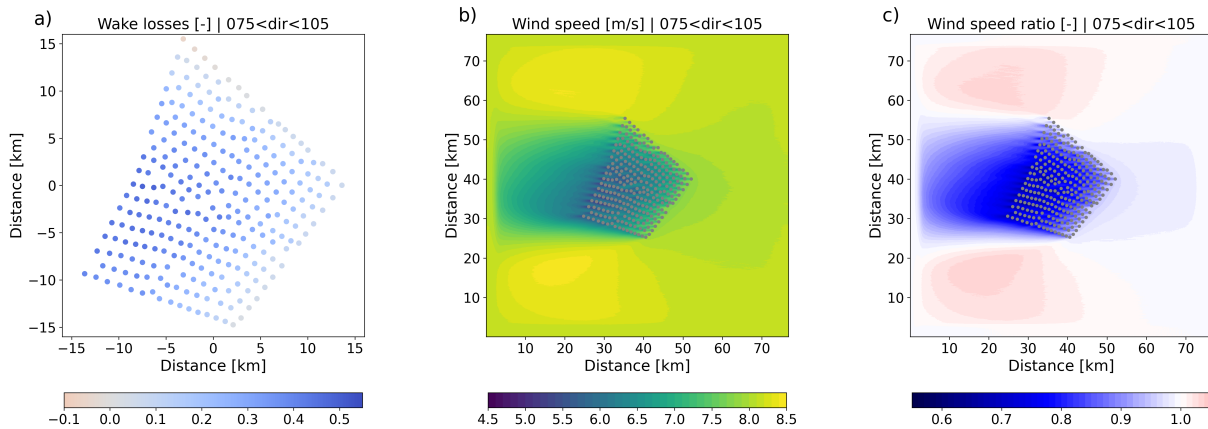
Figure 16. As Fig. 12, but for the IJVer scenario, only including wind directions between 75 and 105 degrees.

first-row losses compared to unstable conditions. Moreover, going deeper into the wind farm, losses increase faster for stable than for unstable conditions: near the southern edge of wind farm turbine losses increase to around 60 % for stable conditions, while being confined to approximately 40 % in convective conditions.

5 Discussion and sensitivity study

To assess production numbers and aerodynamic losses for a suite of hypothetical 4 GW offshore wind farms, a full year of simulations with the LES model GRASP have been performed. Even while GRASP has a relatively high computational
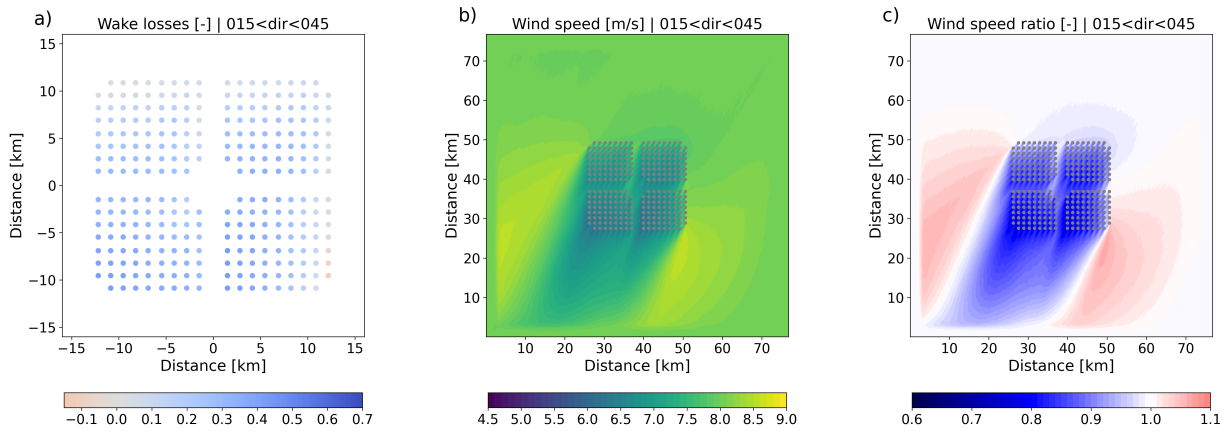
Figure 17. As Fig. 12, but only including unstable conditions, wind speeds between 6 and 10 ms^{-1}, and wind directions between 15 and 45 degrees.
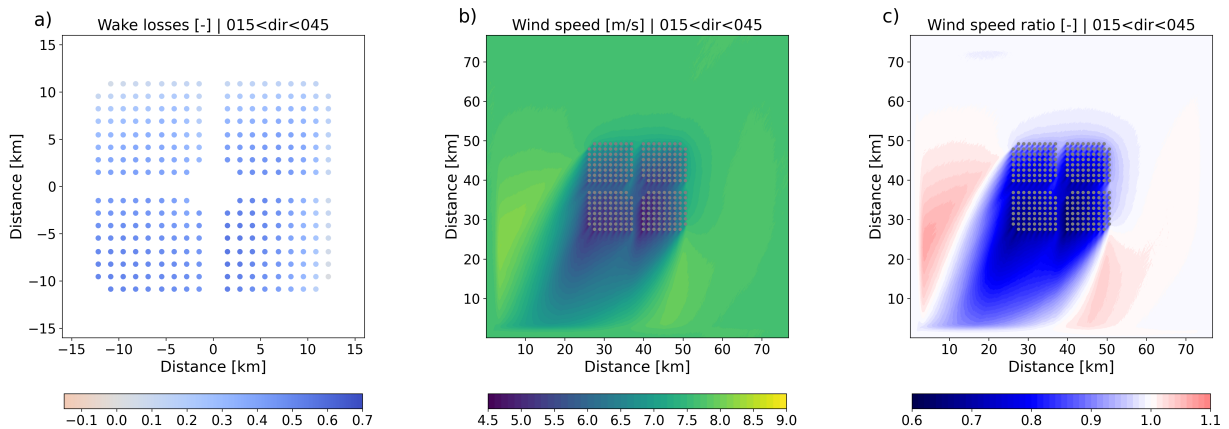
Figure 18. As Fig. 12, but only including stable conditions, wind speeds between 6 and 10 ms^{-1}, and wind directions between 15 and 45 degrees.

performance due to its implementation on GPU's, the computational costs of the simulations are significant. That is to say, in order to enable the atmospheric simulations of large wind farms covering an entire year, the configuration of both the model grid and the domain need to be carefully selected to limit computational cost while maintaining physically sound results.

Because the applied horizontal grid spacing of 120 m might be considered coarse for an atmospheric LES model and/or for the actuator disk model that is used, we consider an assessment of the sensitivity of the modeling results appropriate. Therefore, additional simulations have been performed in which we varied the resolution, the prefactor of the subgrid model

380

(governing the magnitude of the subgrid diffusion), and the domain size (both height and horizontal extent). The sensitivity experiments were performed on a smaller domain of 30720 m. A wind farm of around 770 MW was included. To assess if relative differences between scenarios remained the same, each sensitivity experiment was carried out twice: one time with 72 of the IEA10 turbines (regular 9 by 8 array, spacing of 5.6D), and one time with 36 of the Scaled21 turbines (regular 6 by 6 array, spacing of 5.8D). The sensitivity experiments were not run for the entire year, but for a representative subset of 100 days. The 100 days were selected by a k-means clustering method based on the daily mean of the longitudinal and latitudinal components of the ERA5 100 m wind.

Specifically, the following sensitivity experiments have been performed:

- REF: reference simulation on a 30720 m domain of 3000 m height. The horizontal grid-spacing was 120 m, the height of lowest grid box 30 m (as in the main simulations). Number of grid points: 256 in the horizontal, 48 in the vertical.

- HR: as REF but with the horizontal grid-spacing set to to 60 m. To keep the domain size the same, the number of grid point in the horizontal was increased to 512.

- C_s: as REF but with the c_s prefactor of the subgrid eddy-diffusivity increased by 50 % (see equation 5).

- L_z: as REF but with the domain height increased to 6000 m using 68 vertical levels.

- L_x: as REF but with a twice as large horizontal domain of 61440 m using 512 grid points in the horizontal.

Modifying the modeling set-up may impact both on the ambient conditions (which will change the thrustless production numbers) and the interaction between the turbines of the wind farm (changing the aerodynamic losses). Fig. 19 presents the fractional differences between each sensitivity experiment and the REF experiment. Diffrences in free stream (thrustless) production are less than 0.5 %. Actual production numbers deviate a bit more, but are mostly within 1 % of the REF simulation. Changes in the production number are directly related to the aerodynamic losses: for a similar thrustless production, a reduction of 1 % in actual production equals a 1 % increase in the aerodynamic loss. Naturally, the losses in the sensitivity experiment are smaller than in the main simulations as the installed capacity is smaller.

Increasing the resolution from 120 to 60 m leads to slighty lower aerodynamic losses. This is expected as at finer resolution turbine wakes are more accurately resolved and less smeared out over the grid. Still, the impact is relatively small, especially given the factor of eight difference in computational cost (number of points in the domain and a 50 % reduction in the model time step). Increasing the prefactor of the subgrid eddy-diffusivity c_s by 50 % increases the subgrid diffusion, logically leading to a decrease in resolved fluctuations. As shown by the c_s experiment, the impact on the aerodynamic losses is small. A common way to assess the validity of a large-eddy simulation is to consider the fraction of resolved turbulence. In our main simulation, the resolved fraction of the momentum flux is larger than 80 % for 70 % of the time. For stably-stratified conditions the contribution of the subgrid fluxes is larger, but situations where all turbulent fluctuations dissappear are rare. In practice, a relatively large (fractional) subgrid contribution may have limited effect, as the absolute values of the turbulent fluxes are small. Increasing the horizontal and vertical extent of the domain both have a small impact on the prouction numbers and aerodynamic losses of less than 1 %.
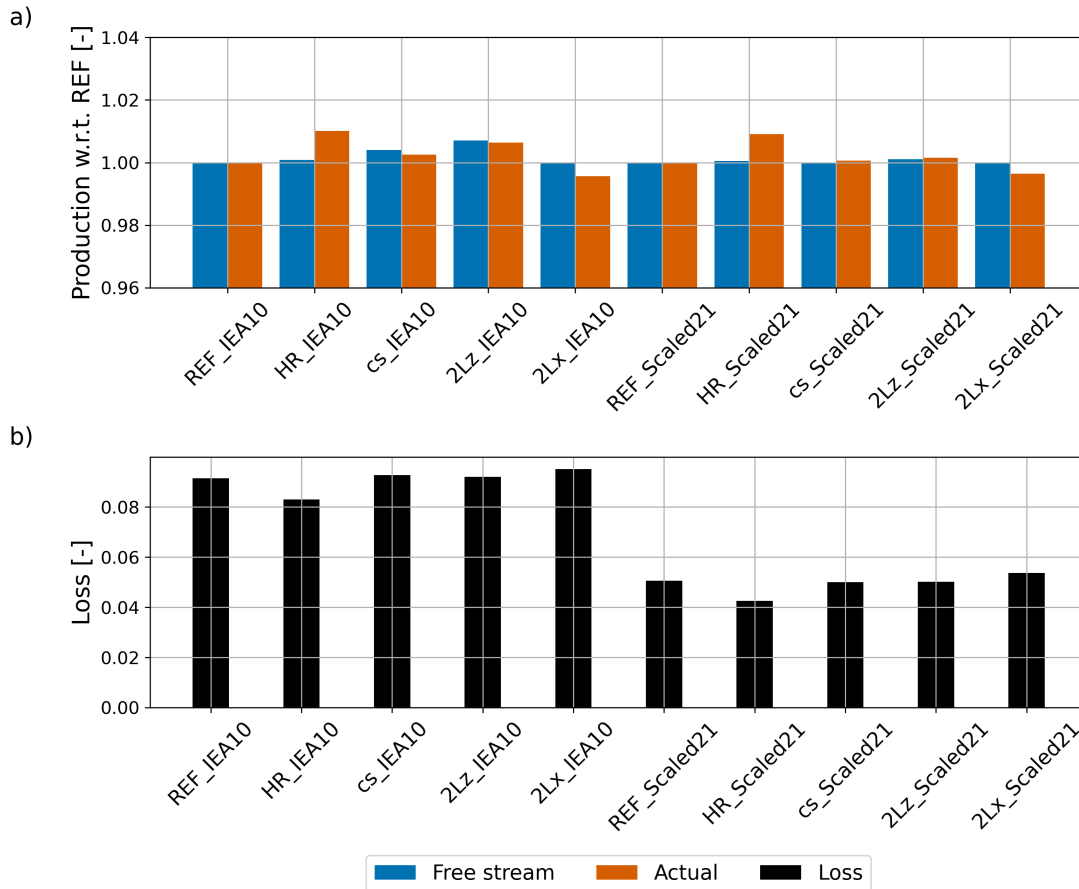
Figure 19. Fractional difference in both thrustless and actual production between the sensitivity experiments and REF (a). Aerodynamic losses (b).

The sensitivity experments were performed for two contrasting wind farm scenarios in order to verify the robustness of the relative differences between the scenarios. Figure 19b indicates that while the aerodynamic losses may change a bit between the sensitivity experiments, the two scenarios show similar patterns. This gives confidence in the comparison between different scenarios in Section 4.

It can be argued that the impact of the sensitivity experiments as discussed above is masked by the fact that for wind speed above 14 ms^{-1} (related to 50 % of the production) losses are negligble anyway (cf. Fig. 6). Therefore, Fig. 20 presents fractional aerodynamic losses for disk-averaged wind speeds between 6 and 10 ms^{-1}. As expected, aerodynamic losses for this specific wind speed range are higher than the overall losses, as are the differences between the scenarios. Still differences with the REF simulations remain within reasonable limits. Presented numbers are for the three stability classes defined above.

The differences between the stability classes are similar for the different sensitivity experiments. This gives confidence in the
425 analysis on the impact of stability in the main results section.
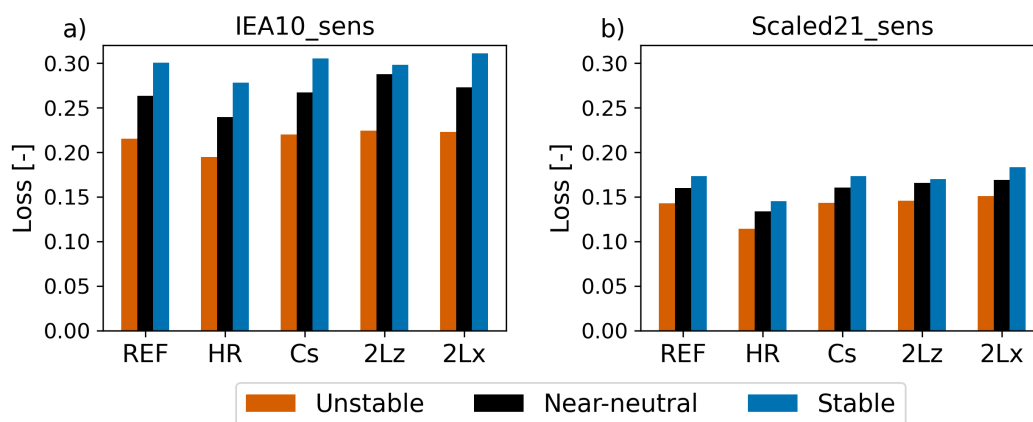
Figure 20. Stability-dependent aerodynamic losses for disk-averaged wind speeds between 6 and 10 ms^{-1} for the IEA10 (a) and Scaled21
(b) sensitivity experiments.

The sensitivity experiments discussed here, give a clear indication of the robustness of the presented results: modyfying grid
spacing, subgrid settings, and extent of the domain within reasonable margins, will likely change the results to several percents
at maximum. Overall, we argue that the sensitivity experiments presented here, do no invalidate the reasoning and conclusions
discussed in the Results Section.

430 Also, from a broader perspective, the sensitivities described here are not larger than, for instance, sensitivies that are reported
in studies with mesoscale models that use wind farm parameterizations like the Fitch et al. (2012) parameterization and/or the
explicit wake parameterization of Volker et al. (2015) as discussed in, for example, Pryor et al. (2019) and Fischereit et al.
(2022). In addition, engineering models rely on calibration on wind farms with much smaller installed capacities as discussed
in the present work and extrapolation to large wind farms is not straightforward. For example, Maas and Raasch (2022)
435 demonstrate that flow dynamics for multi-gigawatt wind farms may differ significantly from smaller-scale wind farms.

6 Conclusions

In this work we studied production numbers and aerodynamic losses for six hypothetical 4 GW offshore wind farm scenarios
using the GRASP large-eddy simulation model. The six scenarios differed in terms of applied turbine type (eg 2n times 10
MW turbines versus n time 20 MW turbines), installed capacity density (5 MWkm^{-2} versus 10 MWkm^{-2}), and layout. For
440 each scenario, a one-year GRASP simulation was performed using 2015 meteorological large-scale conditions taken from
ECMWF's ERA5 reanalysis dataset.

The results suggest that, for the simulated year, aerodynamic losses for a 4 GW offshore wind farm vary from 12 % for 21 MW tubines to 18 % for 10 MW turbines. Moreover, even for turbine types with similar rated capacity but slighty different power- and thrustcurves, energy production may vary by as much as 7.7 %.

445 For all considered scenarios, 80 % of the aerodynamic losses occurs in a narrow wind speed range of 8 to 12 ms^{-1}. On the other hand, 50 % of the energy production occurs without any aerodynamic losses, when all turbines operate at rated capacity. Naturally, these specific numbers should be viewed in context of the considered wind speed probability density function and the wind turbine design choices (power curves).

Although wind speed is identified as the most important factor determining aerodynamic losses, we were able to isolate
450 the impact of stability. A fair assessment of this impact seemed possible by only considering wind speeds between 6 and 10 ms^{-1}. In this wind speed range, aerodynamic losses may be 10 % larger for stably-stratified conditions compared to convective conditions. Numbers vary per scenario with larger differences for scenarios with higher overall losses.

Losses of first-row turbines, which are related to the global blockage effect, were found to be 2 to 3 % in general. These values are consistent with values of the blockage effect reported in literature. As for the general losses, also the first-row
455 losses occur in a narrow range of disk-averaged wind speed. Also, a clear impact of stability is identified. For example, for disk-averged wind speeds between 6 and 10 ms^{-1}, first-row losses may increase to almost 10 % in stably-stratified conditions.

The complexity of disentangling the effect of wind speed and stability is illustrated by considering direction-dependent aerodynamic losses. Only when selecting proper wind speed conditions, a clear impact of stability and of the geometry of the respective scenarios becomes apparent. For instance, when the flow is facing the corners of a square-shaped wind farm, losses
460 are clearly lower than when the flow is directed towards the faces of the wind farm.

Sensitivity experiments were carried out to better understand the impact of various modelling choices such as resolution and domain height. Results suggest that overall energy production varies with 1 to 2 % depending on model settings and/or the domain configuration. Relative differences between the IEA10MW and Scaled21MW turbine scenario are robust.

In summary, using a high-fidelity modeling technique, the results presented in this explorative study provide a clear indi-
465 cation of the performance of future, multi-gigawatt wind farms for one year of realistic weather conditions. Further research could address several open questions like the influence of the lateral boundary conditions, inter-wind farm wake effects and more validation against meteorological observations and wind farm data. More elaborate validation studies can also shed more light into the resolution dependence of the aerodynamic losses.

Data availability. The GRASP large-eddy simulation dataset is available from the authors on request.

470 *Author contributions.* PB performed the model simulation, analyzed the results and wrote the manuscript. RV, PvD, and HJ provided ideas, corrections and modifications. PvD implemented and calibrated the Actuator Disk Model. HJ is main developer of the GRASP model.

Competing interests. The authors have no conflicts of interest to declare that are relevant to the content of this article.

Acknowledgements. The authors would like to acknowledge funding from the Topconsortia for Knowledge and Innovation (TKI) funded Winds of the North Sea in 2050 (WINS50) project. The MSc projects of Sebastiaan Ettema and Thijs Bon (Delft University of Technology)
475 on the global-blockage phenomenon provided inspiration and insights for the present work.

References

Bleeg, J., Purcell, M., Ruisi, R., and Traiger, E.: Wind farm blockage and the consequences of neglecting its impact on energy production, Energies, 11, https://doi.org/10.3390/en11061609, 2018.

Böing, S.: The interaction between deep convective clouds and their environment, Ph.D. thesis, TU Delft, https://doi.org/doi:10.4233/uuid:aa9e6037-b9cb-4ea0-9eb0-a47bf1dfc940, 2014.

Calaf, M., Meneveau, C., and Meyers, J.: Large eddy simulation study of fully developed wind-turbine array boundary layers, Physics of Fluids, 22, 1–16, https://doi.org/10.1063/1.862466, 2010.

Charnock, H.: Wind stress on a water surface, Quarterly Journal of the Royal Meteorological Society, 81, 639–640, 1955.

ECMWF: IFS Manual Part IV: Physical Processes. IFS Documentation Cy43R3, Tech. rep., ECMWF, https://www.ecmwf.int/en/elibrary/17736-part-iv-physical-processes, 2017.

European Commission: Offshore Renewable Energy Strategy, https://energy.ec.europa.eu/topics/renewable-energy/eu-strategy-offshore-renewable-energy_en, 2020.

Fischereit, J., Brown, R., Gia Larsen, X., Badger, J., and Hawkes, G.: Wind farm wakes simulated using WRF, Boundary-Layer Meteorology, 182, 175–224, 2022.

Fitch, A., Olson, J., Lundquist, J., Dudhia, J., Gupta, A., Michalakes, J., and Barstad, I.: Local and mesoscale impacts of wind farms as parameterized in a mesoscale NWP Model., Mon Weather Rev, 140, 3017–3038, https://doi.org/10.1175/MWR-D-11-00352.1, 2012.

Hersbach, H., Bell, B., P., B., Hirahara, S., Horányi, A., Muñoz-Sabater, J., Nicolas, J., Peubey, C., Radu, R., Schepers, D., Simmons, A., Soci, C., Abdalla, S., Abellan, X., Balsamo, G., Bechtold, P., Biavati, G., Bidlot, J., Bonavita, De Chiara, G., Dahlgren, P., Dee, D., Diamantakis, M., Dragani, R., Flemming, J., Forbes, R., Fuentes, M., Geer, A., Haimberger, L., Healy, S., Hogan, R., Hólm, E., Janisková, M., Keeley, S., Laloyaux, P., Lopez, P., Lupu, C., Radnoti, G., De Rosnay, P., Rozum, I., Vamborg, F., Villaume, S., and Thépaut, J.: The ERA5 global reanalysis., Quarterly Journal of the Royal Meteorological Society, 146, 1999–2049, https://doi.org/10.1002/qj.3803, 2020.

Heus, T., Van Heerwaarden, C. C., Jonker, H. J. J., Siebesma, A. P., Axelsen, S., Van Den Dries, K., Geoffroy, O., Moene, A. F., Pino, D., De Roode, S. R., and Vila-Guerau de Arellano, J.: Formulation of the Dutch Atmospheric Large-Eddy Simulation (DALES) and overview of its applications, Geoscientific Model Development, 3, 415–444, https://doi.org/10.5194/gmd-3-415-2010, 2010.

Maas, O. and Raasch, S.: Wake properties and power output of very large wind farms for different meteorological conditions and turbine spacings: A large-eddy simulation case study for the German Bight, Wind Energy Science, 7, 715–739, https://doi.org/10.5194/wes-7-715-2022, 2022.

Mehta, D., van Zuijlen, A. H., Koren, B., Holierhoek, J. G., and Bijl, H.: Large Eddy Simulation of wind farm aerodynamics: A review, Journal of Wind Engineering and Industrial Aerodynamics, 133, 1–17, https://doi.org/10.1016/j.jweia.2014.07.002, 2014.

Meyers, J. and Meneveau, C.: Large Eddy Simulations of Large Wind-Turbine Arrays in the Atmospheric Boundary Layer, 48th AIAA Aerospace Sciences Meeting Including the New Horizons Forum and Aerospace Exposition, pp. 1–10, https://doi.org/10.2514/6.2010-827, 2010.

Neggers, R. A. J., Siebesma, A. P., and Heus, T.: Continuous single-column model evaluation at a permanent meteorological supersite, Bulletin of the American Meteorological Society, 93, 1389–1400, https://doi.org/10.1175/BAMS-D-11-00162.1, 2012.

Porté-Agel, F., Bastankhah, M., and Shamsoddin, S.: Wind-Turbine and Wind-Farm Flows: A Review, Boundary-Layer Meteorology, 174, 1–59, https://doi.org/10.1007/s10546-019-00473-0, 2020.

Pryor, S., Shepard, T., Bartherlmie, R., Hahmann, A., and Volker, P.: Wind farm wakes simulated using WRF, Journal of physics: Conf. Series, 1256, https://doi.org/10.1088/1742-6596/1256/1/012025, 2019.

Rozema, W., Bae, H. J., Moin, P., and Verstappen, R.: Minimum-dissipation models for large-eddy simulation, Physics of Fluids, 27, https://doi.org/10.1063/1.4928700, 2015.

RVO: General Information IJmuiden Ver, https://offshorewind.rvo.nl/cms/view/5c06ac88-c12f-4903-89f3-27d66937b7e9/general-information-ijmuiden-ver, 2022.

Schalkwijk, J., Griffith, E. J., Post, F. H., and Jonker, H. J. J.: High-performance simulations of turbulent clouds on a desktop PC, Bulletin of the American Meteorological Society, 93, 307–314, 2012.

Schalkwijk, J., Jonker, H., Siebesma, A., and Van Meijgaard, E.: Weather forecasting using GPU-based large-Eddy simulations, Bulletin of the American Meteorological Society, 96, https://doi.org/10.1175/BAMS-D-14-00114.1, 2015a.

Schalkwijk, J., Jonker, H. J. J., Siebesma, A. P., and Bosveld, F. C.: A Year-Long Large-Eddy Simulation of the Weather over Cabauw: an Overview, Monthly Weather Review, 143, 828–844, https://doi.org/10.1175/MWR-D-14-00293.1, 2015b.

Schneemann, J., Theuer, F., Rott, A., Dörenkämper, M., and Kühn, M.: Offshore wind farm global blockage measured with scanning lidar, Wind Energy Science, 6, 521—-538, https://doi.org/10.5194/wes-6-521-2021, 2021.

Stevens, R. J. and Meneveau, C.: Flow Structure and Turbulence in Wind Farms, vol. 49, https://doi.org/10.1146/annurev-fluid-010816-060206, 2017.

Stevens, R. J., Graham, J., and Meneveau, C.: A concurrent precursor inflow method for Large Eddy Simulations and applications to finite length wind farms, Renewable Energy, 68, 46–50, https://doi.org/10.1016/j.renene.2014.01.024, 2014.

Strickland, J., Srinidhi, N., and Stevens, R.: Wind farm blockage in a stable atmospheric boundary layer, Renewable Energy, 197, 50–58, https://doi.org/10.1016/j.renene.2022.07.108, 2022.

The Esbjerg Declaration: The Esbjerg Declaration on The North Sea as a Green Power Plant of Europe, https://www.rijksoverheid.nl/documenten/publicaties/2022/05/18/the-esbjerg-declaration-on-the-north-sea-as-a-green-power-plant-of-europe, 2022.

Veers, P., Dykes, K., Lantz, E., Barth, S., Bottasso, C. L., Carlson, O., Clifton, A., Green, J., Green, P., Holttinen, H., Laird, D., Lehtomäki, V., Lundquist, J. K., Manwell, J., Marquis, M., Meneveau, C., Moriarty, P., Munduate, X., Muskulus, M., Naughton, J., Pao, L., Paquette, J., Peinke, J., Robertson, A., Rodrigo, J. S., Sempreviva, A. M., Smith, J. C., Tuohy, A., and Wiser, R.: Grand challenges in the science of wind energy, Science, 366, eaau2027, https://doi.org/10.1126/science.aau2027, 2019.

Verzijlbergh, R. A.: Atmospheric flows in large wind farms, Europhysics News, 52, 20–23, https://doi.org/10.1051/epn/2021502, 2021.

Volker, P., Badger, J., Hahmann, A., and Ott, S.: The explicit wake parametrisation V1.0: a wind farm parametrisation in the mesoscale model WRF, Geosci Model Dev, 8, 3715–3731, https://doi.org/10.5194/gmd-8-3715-2015, 2015.

Wu, K. and Porté-Agel, F.: Flow Adjustment Inside and Around Large Finite-Size Wind Farms, Energies, 10, 2164, https://doi.org/10.3390/en10122164, 2017.